

Supporting Information

**Hollow carbon nanoreactors integrating NiFe-LDH
nanodots with adjacent La single atoms for efficient
oxygen electrocatalytic reactions**

Leilei Yin^{a,b}, Yuyan Liu^c, Shuai Zhang^b, Yongkang Huang^c, Qiang Wang^{a*}, Jin-
Cheng Liu^{b*}, Chao Gu^b, Yaping Du^{b*}

^a Inner Mongolia Academy of Science and Technology, Hohhot, Inner Mongolia 010010,
China.

^b Tianjin Key Lab for Rare Earth Materials and Applications, Center for Rare Earth and
Inorganic Functional Materials, School of Materials Science and Engineering, National
Institute for Advanced Materials, Nankai University, Tianjin 300350, China.

^c College of Chemistry, Nankai University, Tianjin 300071, China.

E-mail: ypdu@nankai.edu.cn; liujincheng@nankai.edu.cn; wangqiang@imast.ac.cn

Experimental section

Reagents: zinc nitrate hexahydrate ($\text{Zn}(\text{NO}_3)_2 \cdot 6\text{H}_2\text{O}$), nickelous nitrate hexahydrate ($\text{Ni}(\text{NO}_3)_2 \cdot 6\text{H}_2\text{O}$), iron nitrate nonahydrate ($\text{Fe}(\text{NO}_3)_2 \cdot 9\text{H}_2\text{O}$), lanthanum acetate sesquihydrate, 2-methylimidazole, melamine, sulfur powder, potassium hydroxide were purchased from Aladdin. Ethanol, Iso-Propyl Alcohol were obtained from Macklin. Commercial Pt/C and RuO_2 were obtained from Johnson Matthey. Milli-Q water with the specific resistance of $18.2 \text{ M}\Omega \text{ cm}$ was obtained by reversed osmosis followed by ion-exchange and filtration. All reagents were used as required without purification steps.

Preparation of ZIF-8: Typically, 60 mL of 2-methylimidazole in methanol solution (0.48 M) was mixed with 60 mL of $\text{Zn}(\text{NO}_3)_2 \cdot 6\text{H}_2\text{O}$ in methanol solution (0.12 M) under vigorous stirring for 12 h at room temperature. The as-obtained precipitates were centrifuged and washed with methanol several times and dried in vacuum overnight at 60°C .

Preparation of NHPC: The obtained white ZIF-8 powder with a mass ratio of 1:1 was mixed with melamine by thorough grinding and transferred into a quartz boat. The mixture was heated to 550°C at a heating rate of 2°C min^{-1} and held for 1 h, followed by heating to 1100°C at a heating rate of 5°C min^{-1} and held for 2 h. The heating process was carried out under argon protection. Non-hollow NC is obtained in the same process, except without melamine.

Preparation of La SNHPC: NHPC powder (30 mg) and lanthanum acetate sesquihydrate (6.8 mg) were co-mixed in 20 mL of deionized water and stirred at room temperature for 12 h. Subsequently, the solid product is obtained by rotary evaporation and thoroughly mixed with sulfur powder (1.8 mg). Then, the mixture was pyrolyzed at 800°C under nitrogen atmosphere for 90 min. The prepared sample was then allowed acid treatment (5 mM H_2SO_4) for 20 min. After sufficient washing and centrifugation, the obtained solid products were dried at 60°C overnight to make the La SNHPC catalyst. Similarly, SNHPC or La NHPC are obtained without the addition of La precursors or sulfur powder, respectively.

Preparation of NiFe-LDH@La SNHPC: La SNHPC (30 mg), $\text{Ni}(\text{NO}_3)_2 \cdot 6\text{H}_2\text{O}$

(25 mg) and $\text{Fe}(\text{NO}_3)_2 \cdot 9\text{H}_2\text{O}$ (12.5 mg) were mixed in 15 mL of deionized water and sonicated for 30 min, immediately followed by slow dropwise addition of 0.1M KOH (3 mL) solution to the mixed solution under continuous stirring. After stirring for 1 hour, the product was centrifuged and washed 3 times with deionized water. The obtained solid products were dried at 60 °C overnight to make the catalyst. As a comparison, SNHPC, La NHPC and NHPC as substrates were used directly to obtain NiFe-LDH@SNHPC, NiFe-LDH@ La NHPC and NiFe-LDH@ NHPC catalyst, respectively. In addition, the same preparation process for NiFe-LDH@La SNC is realized on non-hollow NC.

Characterizations:

The powder X-ray diffraction (XRD) measurements of the as-obtained samples were tested on a Rigaku SmartLab XRD (Rigaku, Japan) with Cu K α radiation ($\lambda = 1.5418 \text{ \AA}$, 3kW). The Field emission scanning electronic microscope (FE-SEM, JSM-7800F, Japan) and High-resolution transmission electron microscope (HRTEM, JEM-2800, Japan) were used to determine the morphologies and sizes of the samples. High-angle annular dark-field scanning transmission electron microscopy (HAADF-STEM) images were obtained at 300 kV with a FEI Titan Cubed Themis G2300. The X-ray photoelectron spectroscopy (XPS) was carried out on Thermo Scientific ESCALAB 250Xi instrument equipped with an Al X-ray excitation source. The metal content of the samples was measured by ICP-OES (Agilent 5110). N_2 adsorption-desorption isotherms were obtained on Micromeritics ASAP2460 at 77 K, and Brunauer-Emmett-Teller (BET) method was used to calculate the surface area. Raman spectra were recorded using a TEO SR-500I-A operating with a laser wavelength of 532 nm. The X-ray absorption fine structure spectra (La L₃-edge) were collected at Spring-8. The storage rings of BSRF were operated at 2.5 GeV with a maximum current of 250 mA. Using Si (111) double-crystal monochromator, the data collection was carried out in transmission mode using ionization chamber. All spectra were collected in ambient

conditions. The acquired EXAFS data were processed according to the standard procedures using the ATHENA module implemented in the IFEFFIT software packages. The EXAFS spectra were obtained by subtracting the post-edge background from the overall absorption and then normalizing with respect to the edge-jump step. Subsequently, Data of La L₃-edge were Fourier transformed to real (R) space using a Hanning windows ($dk=1.0 \text{ \AA}^{-1}$) to separate the EXAFS contributions from different coordination shells. To obtain the quantitative structural parameters around central atoms, least-squares curve parameter fitting was performed using the ARTEMIS module of IFEFFIT software packages.

Computational details:

All density functional theory (DFT) calculations were carried out using the Vienna Ab initio Simulation Package (VASP)¹. The ion-electron interactions were described using the projector-augmented wave (PAW) method^{2,3}. A kinetic energy cutoff of 500 eV was applied for the plane wave expansions with the convergence test in Fig. S39, and the generalized gradient approximation (GGA) with the Perdew-Burke-Ernzerhof (PBE) functional was employed⁴. Gamma-centered Monkhorst-Pack sampling with a grid of $3 \times 3 \times 1$ was utilized for reciprocal space integration⁵ with the convergence test in Fig. S40. The convergence criteria for energy and force were set to 10^{-5} eV and 0.03 eV/\AA , respectively. The Gaussian smearing method was used, and the width of the smearing was set as 0.05 eV. Free energy corrections for all adsorbed species were performed using the VASPKIT package⁶ (Table S3). The Hubbard corrections (DFT+U) for Ni, Fe, and La were set as 5.2, 2.6, and 4.0 eV according to the previous literature which have been extensively benchmarked on thermodynamics⁷⁻¹⁰. The NiFe-LDH@La SNHPC was modeled as a heterostructure of NiFe-LDH and La, S, N co-doped graphene, as shown in Fig. S41. The $p(4 \times 4)$ supercell of monolayer Ni(OH)₂ (001) facet was constructed, in which four Ni atoms were replaced by Fe atoms to achieve a Ni Fe ratio of

3:1, aligning with experimental results. The optimized cell length of NiFe-LDH was 12.76 Å which agrees well with the experimental result⁹, and this parameter was used for heterostructure. The $(3\sqrt{3} \times 3\sqrt{3})R30^\circ$ supercell of graphene with a size of 12.78 Å was constructed to minimize lattice mismatch. Given the absence La-S coordination in the experiment, the S atoms were placed away from the LaN₄ motif, which was constructed as the previous report¹¹. There are a total of 129 atoms in the heterostructure, including 12 Ni atoms, 4 Fe atoms, 32 O atoms, 32 H atoms, 42 C atoms, 1 La atom, 2 S atoms, and 4 N atoms. The initial distance between the two layers was set as 3 Å. To avoid the interaction between periodic slabs, the thickness of vacuum spaces was set more than 15 Å. Part of hydrogen atoms were removed to simulate NiFe oxyhydroxide at oxidation potential.

Electrochemical measurements:

All the electrochemical measurements were carried out in a conventional three-electrode system on a CHI 660E electrochemical station (Shanghai CH Instruments Co., China). The counter electrode and the reference electrode were a platinum sheet electrode and a saturated Hg/HgO electrode, respectively. All the potentials reported were converted to the reversible hydrogen electrode (RHE). The homogeneous catalyst ink was prepared by ultrasonically dispersing 5.0 mg samples in 1.0 mL of a mixture solution containing ethanol (300 µL), water (180 µL) and Nafion (5 wt%, 20 µL). For OER electrochemical tests, the surface area of the working electrode was controlled at 1.0×1.0 cm². For the series of prepared catalysts and the RuO₂ reference sample, the loading amount on the carbon paper is 0.5 mg cm⁻². OER performance was evaluated in O₂-saturated 1.0 M KOH solution. Electrochemical CV cycles were performed prior to all tests to ensure that the catalyst was fully activated. All the potentials of OER polarization curves were obtained with a scan rate of 5 mV s⁻¹ and corrected with the 95%-iR compensation. The overpotential (η) was calculated according to the following formula: $\eta = E(\text{RHE}) - 1.23 \text{ V}$. Electrochemical impedance spectroscopy (EIS)

was carried out by applying an amplitude of 10 mV over the frequency window from 10^6 to 0.01 Hz at a certain potential. The long-term durability was performed through continuously cycling between 1.45 and 1.55 V vs. RHE at a scan rate of 50 mV s^{-1} for 5000 cycles. The C_{dl} is used to estimate the ECSA of the catalyst. It is obtained by testing the CV between 1.175 to 1.275 V vs RHE with a scan rate from 10 mV s^{-1} to 50 mV s^{-1} .

The ORR electrochemical tests were performed in O_2 -saturated 0.1 M KOH solution. A certain volume of the catalyst ink was carefully dropped onto the polished glassy carbon rotating disk electrode (RDE, diameter: 5 mm) with a controlled loading of 0.5 mg cm^{-2} (commercial 20% Pt/C with a loading of $40 \mu\text{g}_{\text{Pt}} \text{ cm}^{-2}$ as a reference). LSV polarization curves were measured with rotating rates from 400 to 2500 rpm with a scan rate of 5 mV s^{-1} . The corresponding electron transfer number and kinetic current density (J_k) were determined from the slope of the linear line according to the following Koutechy-Levich (K-L) equation:

$$\frac{1}{J} = \frac{1}{J_L} + \frac{1}{J_K} = \frac{1}{B\omega^{1/2}} + \frac{1}{J_K}$$

$$B = 0.62nF(D_0)^{2/3}(\nu)^{-1/6}C_0$$

where J , J_L , J_K are the measured current density, diffusion-limiting current density, and kinetic current density, respectively. ω is the angular velocity of the disk ($\omega = 2\pi N$, N is the rotation speed), n is the electron transfer number, F is the Faraday constant ($F = 96485 \text{ C mol}^{-1}$), D_0 is the diffusion coefficient of oxygen ($D_0 = 1.9 \times 10^{-5} \text{ cm}^2 \text{ s}^{-1}$, 0.1 M KOH), C_0 is the bulk concentration of oxygen ($C_0 = 1.2 \times 10^{-6} \text{ mol cm}^{-3}$, 0.1 M KOH), ν is the kinetic viscosity of the electrolyte ($\nu = 0.01 \text{ cm}^2 \text{ s}^{-1}$).

Zn-air battery assembly and measurements:

For Liquid Zinc-air battery, polished zinc foil (0.30 mm thickness) as the anode and aqueous solution containing 6 M KOH+0.2 M Zn (OAc)₂ as the electrolyte. The catalyst slurry was first prepared by mixing NiFe-LDH@La SNHC and commercial 20% Pt/C (mass ratio of 1:1) in Isopropyl Alcohol, followed by uniform drop-coating onto the carbon paper/gas diffusion layer

composite substrate as air cathode. As a result, the catalyst loading was calculated to be 1.0 mg cm^{-2} . Commercial RuO_2 replaced NiFe-LDH@La SNHC as a performance reference under equivalent conditions. The discharge polarization curve performed on CHI-660E with a scan rate of 5 mV s^{-1} . The cyclic stability test was performed using a LAND CT2001A battery test system at 5 mA cm^{-2} with 10 min per cycle (5 min charge and 5 min discharge).

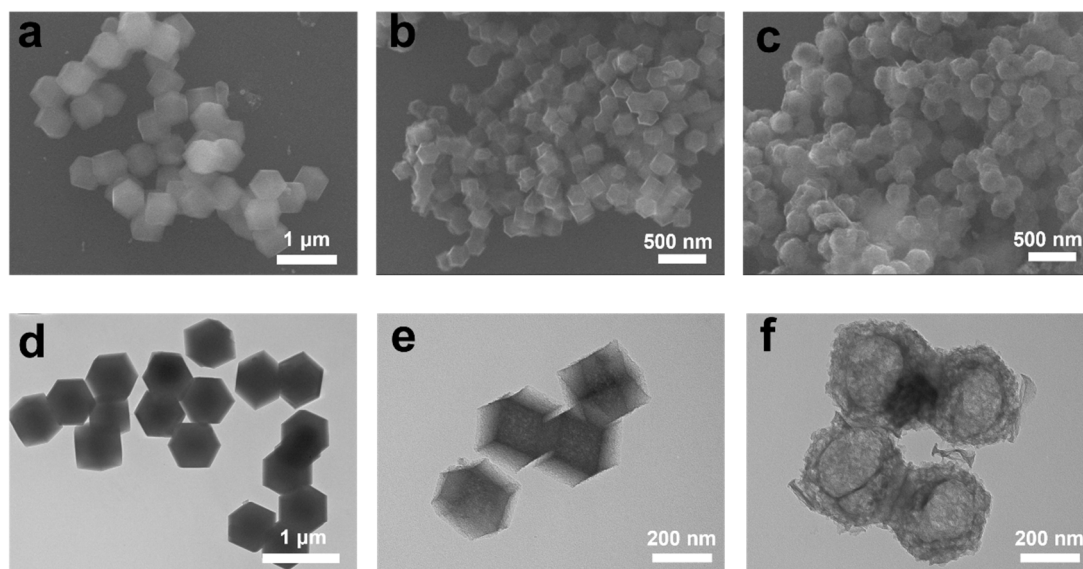


Fig. S1 SEM images (up) and TEM images (down) for ZIF-8 (a, d), NC (b, e), and NHPC (c, f).

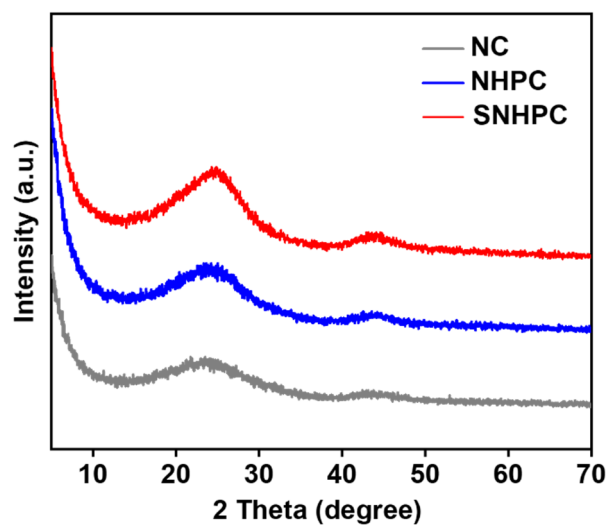


Fig. S2 XRD patterns of different samples.

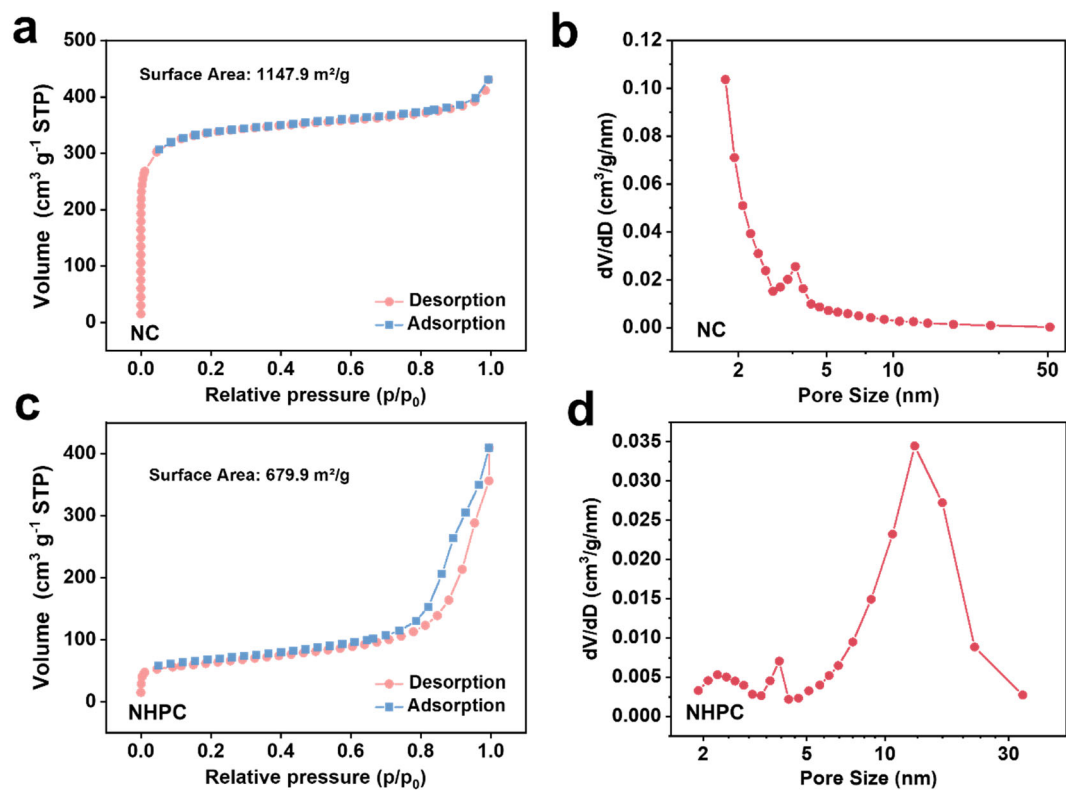


Fig. S3 N_2 adsorption and desorption isotherms (a, c) and pore size distribution curves (b, d) of NC and NHPC.

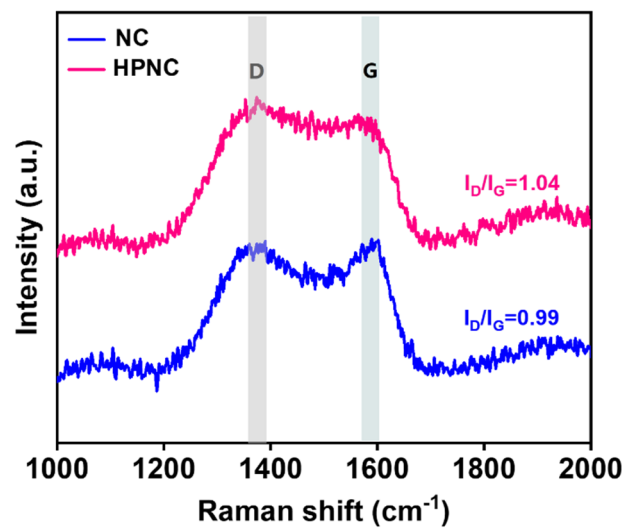


Fig. S4 Raman spectra of NC and NHPC.

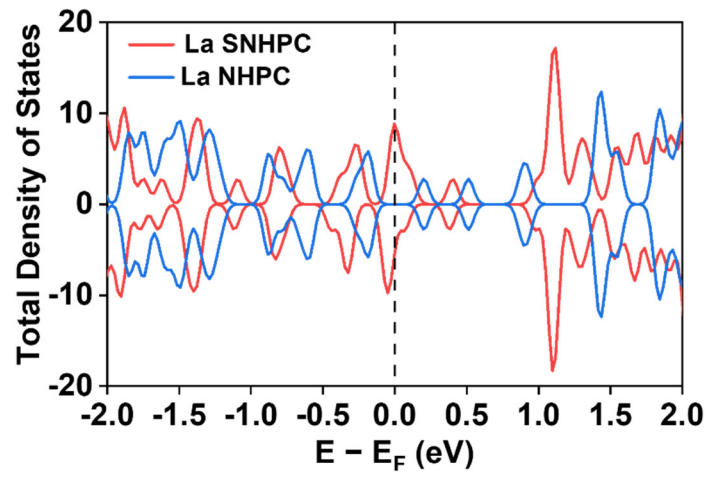


Fig. S5 The calculated total density of states (TDOS) for La SNHPC and La NHPC.

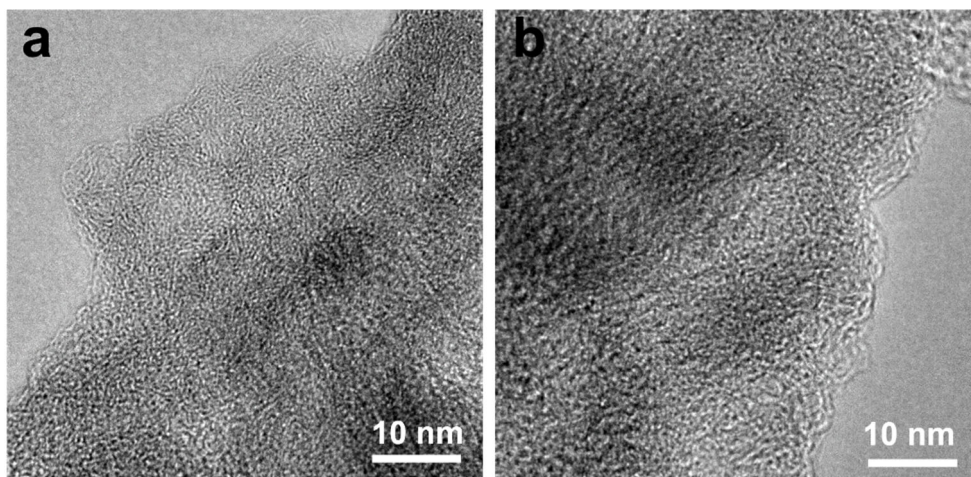


Fig. S6 HRTEM images of La NHPC (a) and La SNHPC (b).

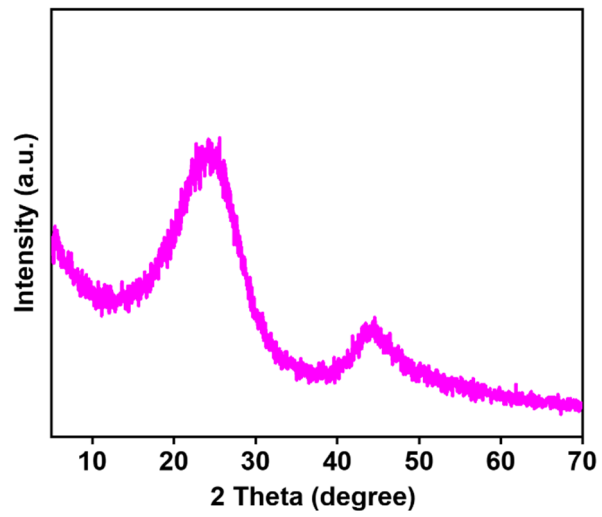


Fig. S7 XRD patterns of La NHPC.

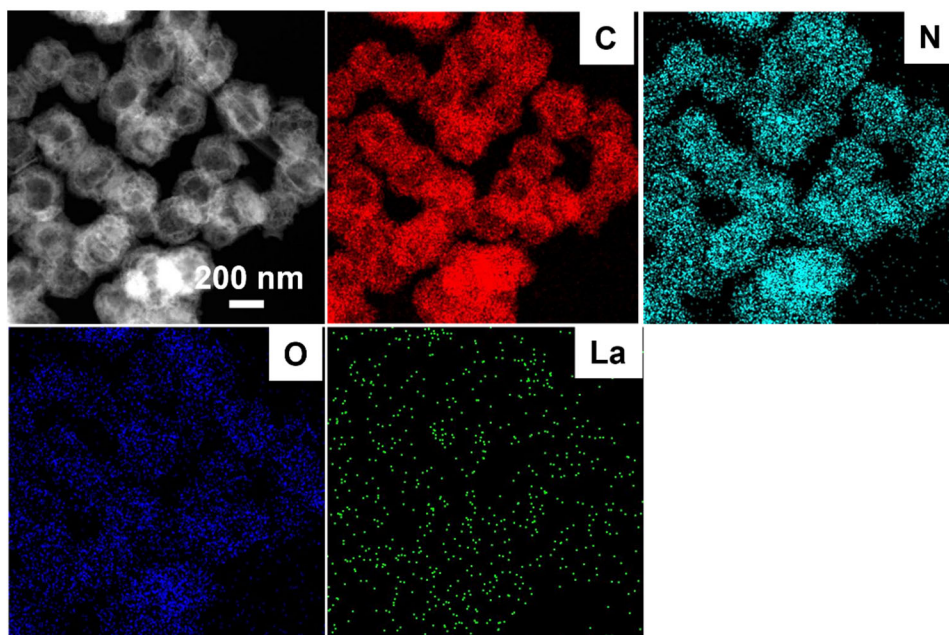


Fig. S8 Dark-field TEM image and corresponding EDS elemental mapping of La NHPC.

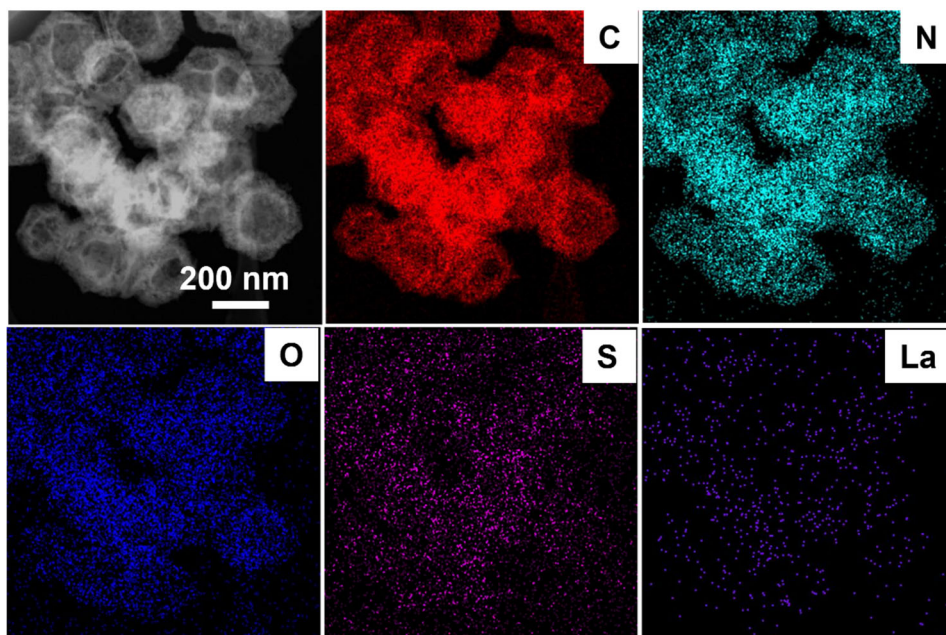


Fig. S9 Dark-field TEM image and corresponding EDS elemental mapping of La SNHPC.

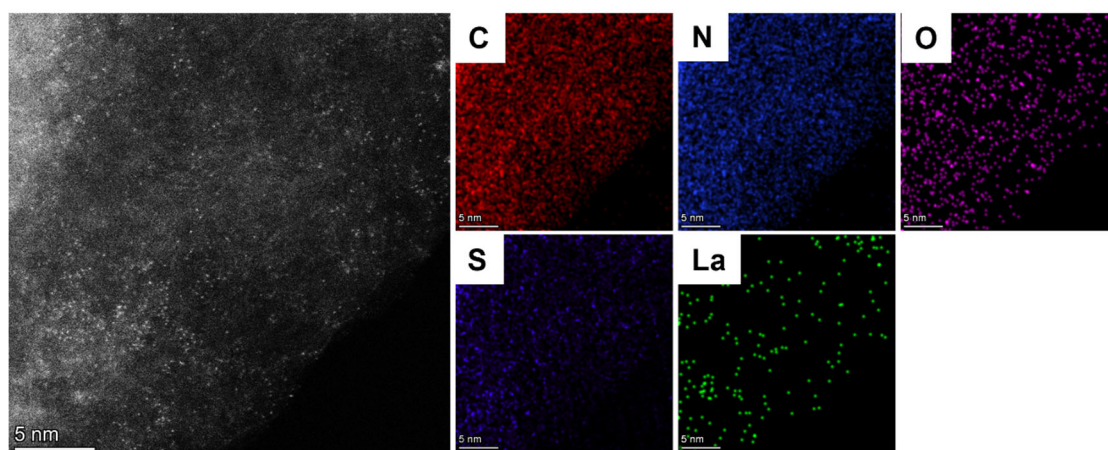


Fig. S10 AC-HAADF-STEM image and corresponding EDS elemental mapping of La SNHPC.

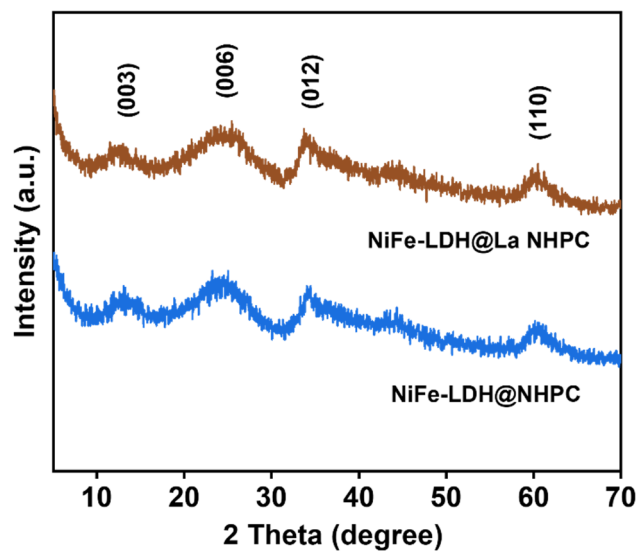


Fig. S11 XRD patterns of different samples.

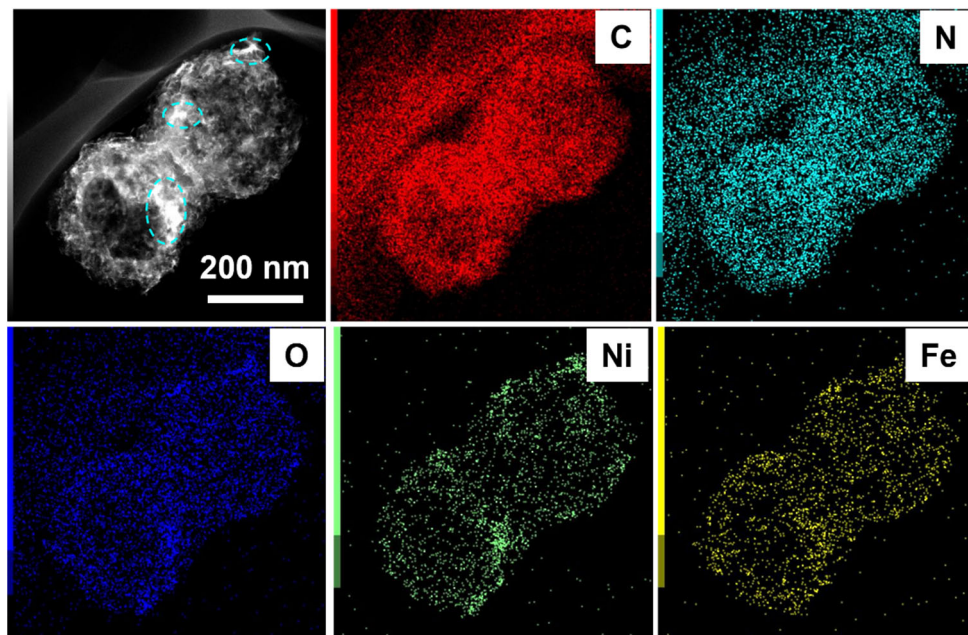


Fig. S12 Dark-field TEM image and corresponding EDS elemental mapping of NiFe-LDH@NHPC.

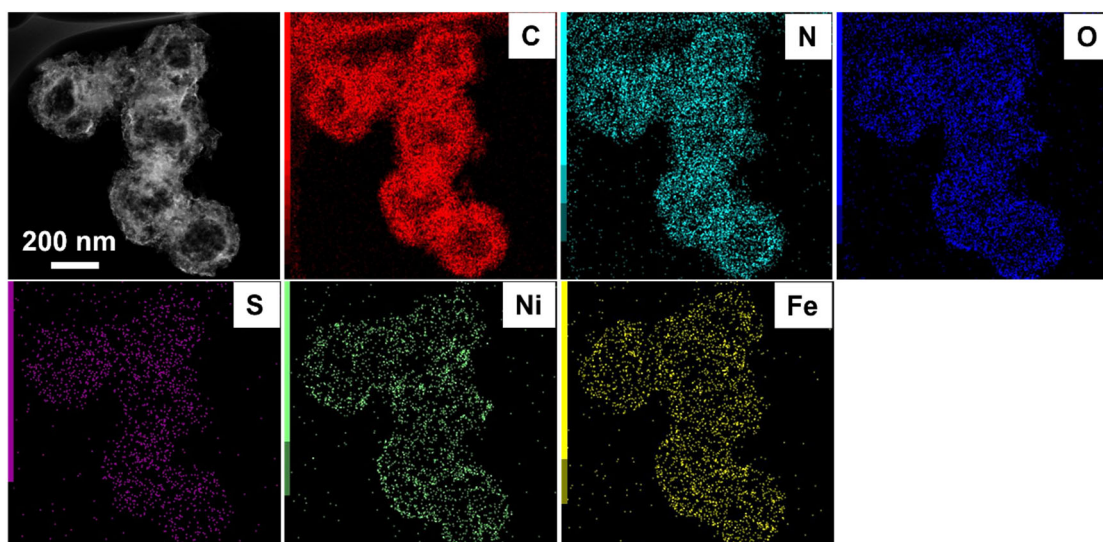


Fig. S13 Dark-field TEM image and corresponding EDS elemental mapping of NiFe-LDH@SNHPC.

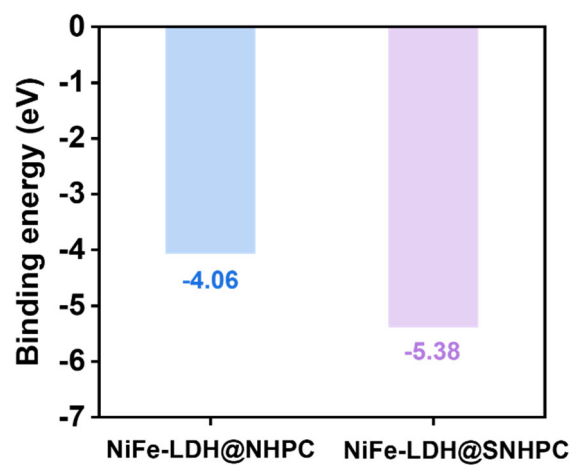


Fig. S14 Binding energies of NiFe-LDH@NHPC and NiFe-LDH@SNHPC, for instance $E_{\text{bind}} = E(\text{NiFe-LDH@NHPC}) - E(\text{NiFe-LDH}) - E(\text{NHPC})$.

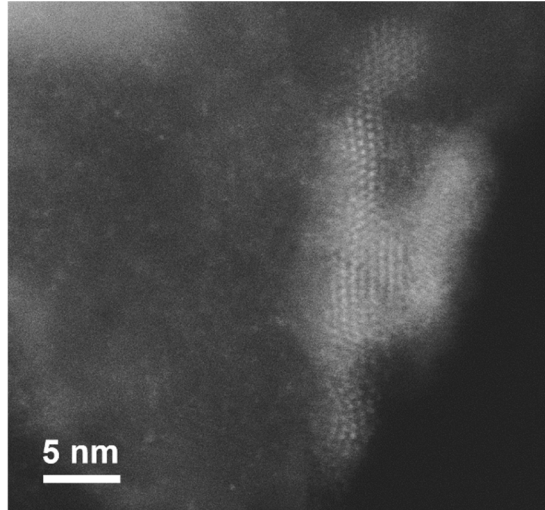


Fig. S15 AC-HAADF-STEM image of NiFe-LDH@SNHPC.

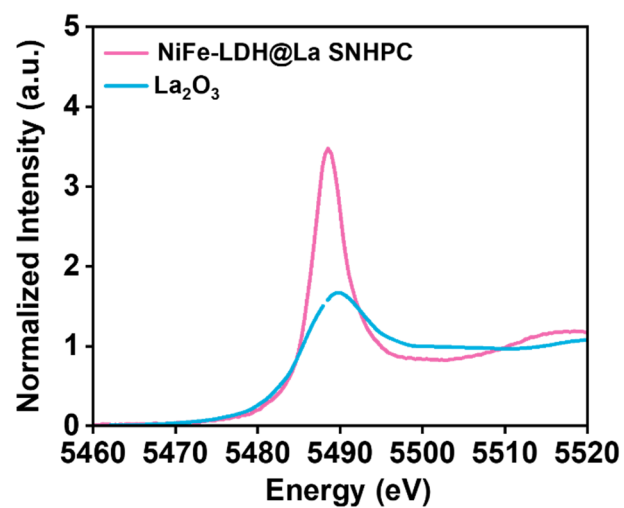


Fig. S16 La L-edge XANES spectra of La₂O₃ and NiFe-LDH@La SNHPC.

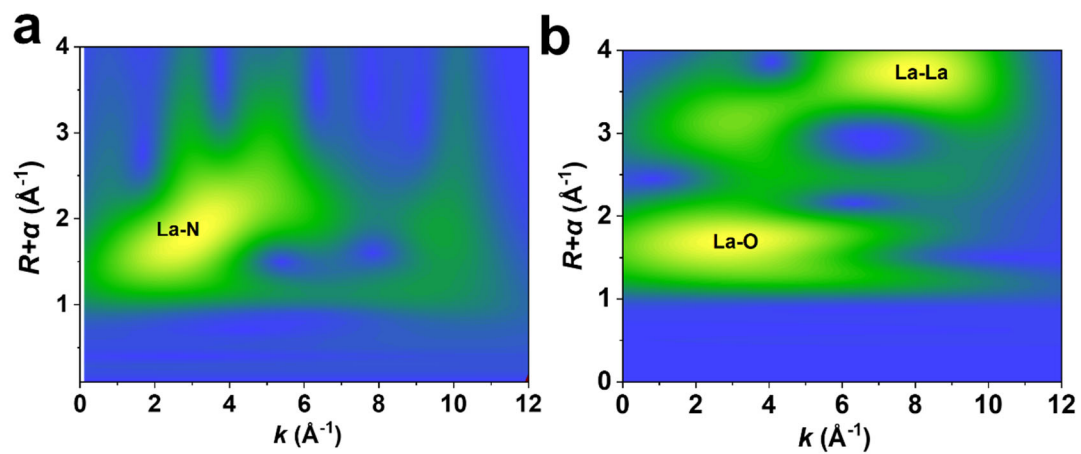


Fig. S17 The wavelet transforms of EXAFS for NiFe-LDH@La SNHPC(a) and La₂O₃(b).

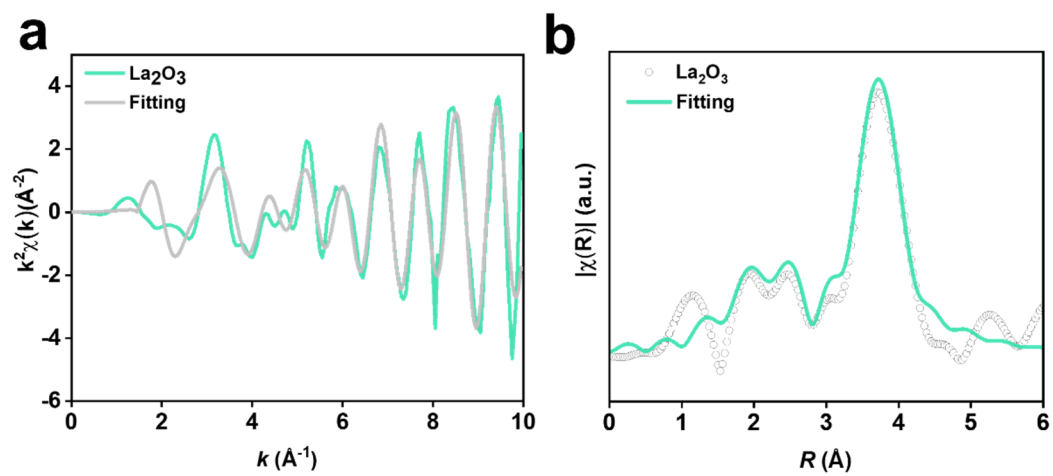


Fig. S18 La L-edge EXAFS fitting curves of La_2O_3 .

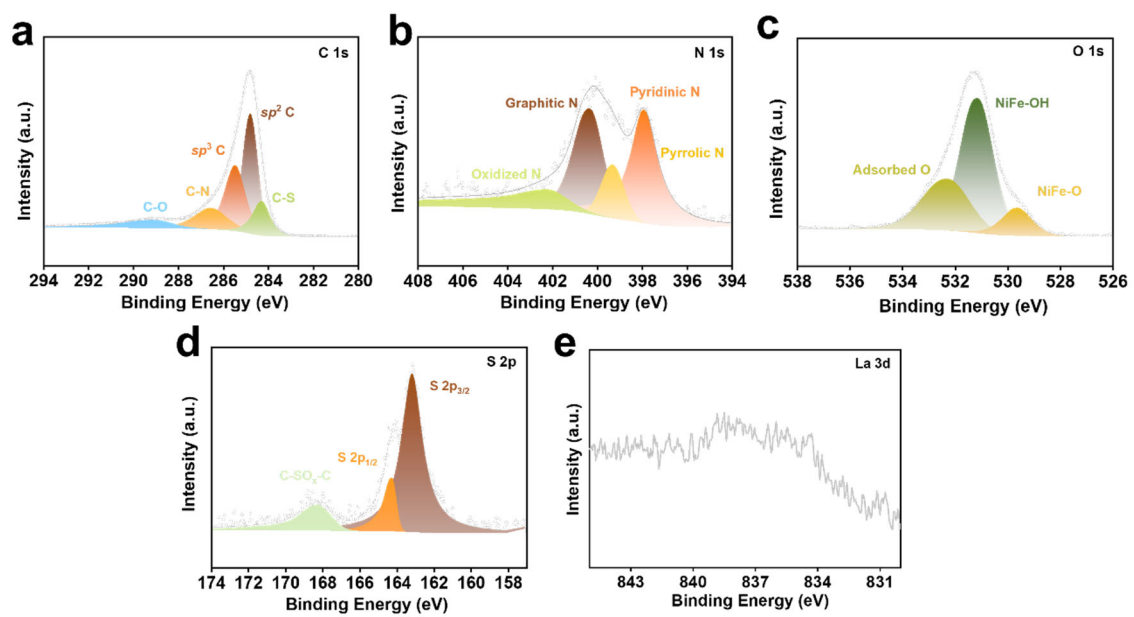


Fig. S19 The High-resolution XPS spectra for C 1s (a), N 1s (b) O 1s (c), S 2p (d), La 3d (e) of NiFe-LDH@La SNHPC.

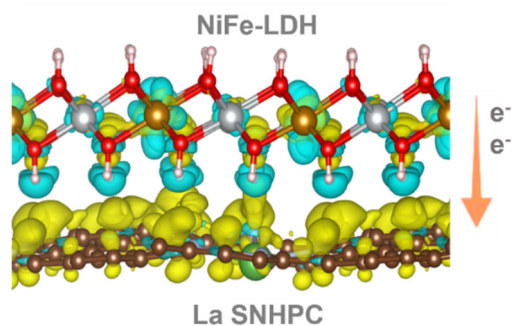


Fig. S20 The charge density difference plots of the NiFe-LDH@La SNHPC heterostructure, where the yellow region represents electron accumulation and the blue region represents electron depletion. The white, coffee, blue, red, yellow, silver, brown, and green balls represent the H, C, N, O, S, Fe, Ni, and La, respectively.

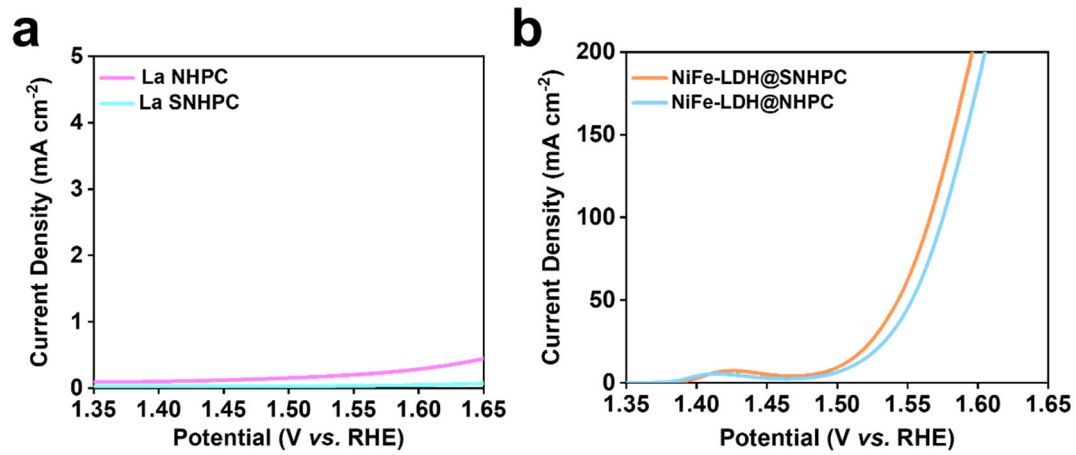


Fig. S21 OER LSV curves of different samples.

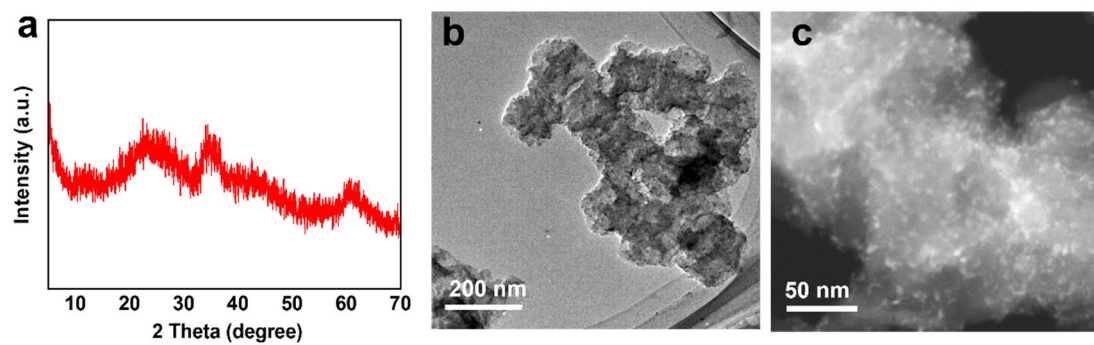


Fig. S22 XRD patterns (a), TEM image (b), and dark-field TEM image (c) of NiFe-LDH@La SNC.

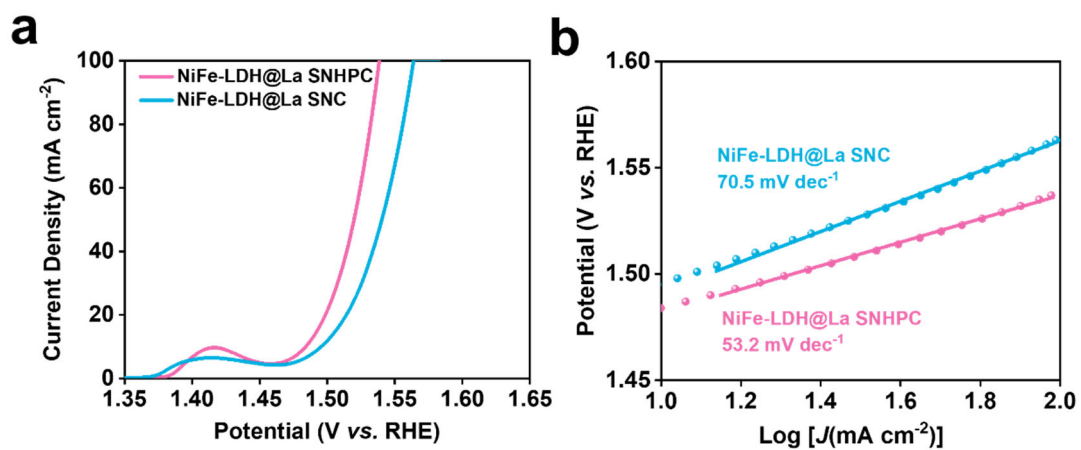


Fig. S23 OER LSV curves (a) and Tafel plots (b) of NiFe-LDH@La SNHPC and NiFe-LDH@La SNC.

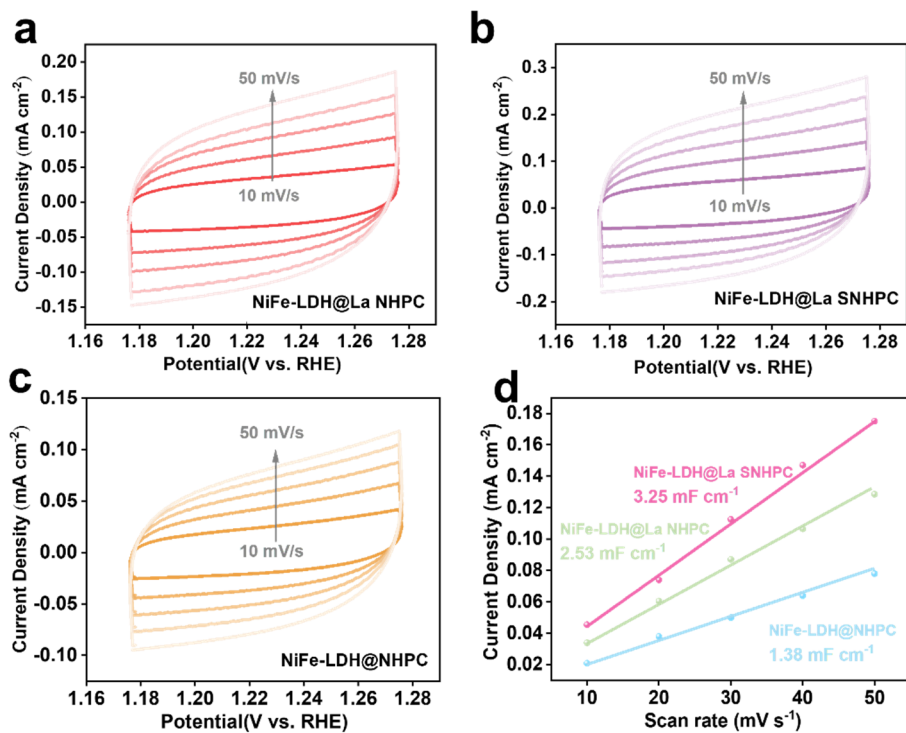


Fig. S24 (a-c) CV curves at different scan rates (10-50 mV s^{-1}) of different samples. (d) C_{dl} value observed from CV plots at different scan rates.

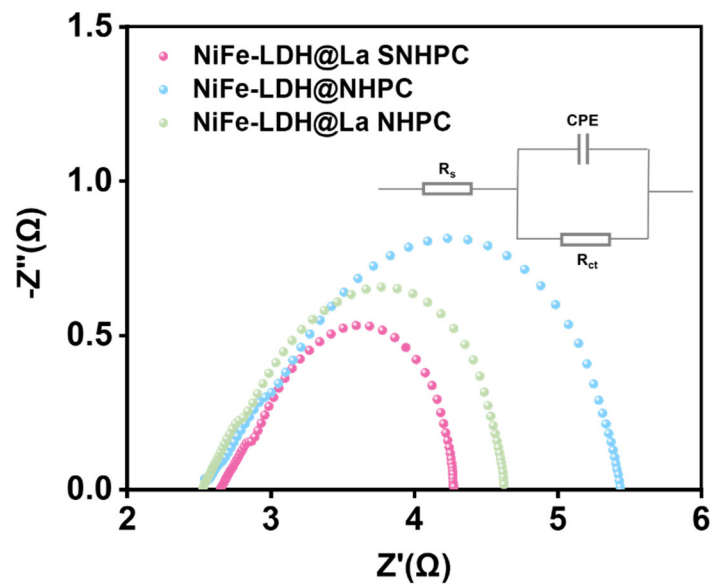


Fig. S25 EIS Nyquist plots of different samples. Inset: equivalent circuit used for fitting the Nyquist curves

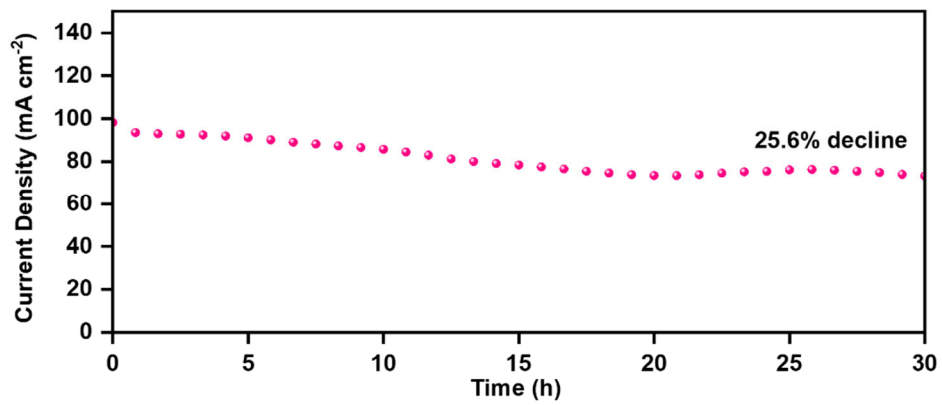


Fig. S26 *i-t* curves for NiFe-LDH@La SNHPC

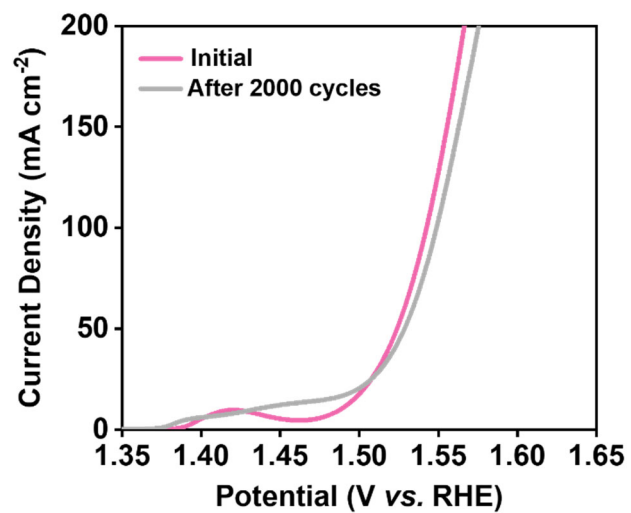


Fig. S27 OER LSV curves of NiFe-LDH@La SNHPC before and after 2000 CV cycles test.

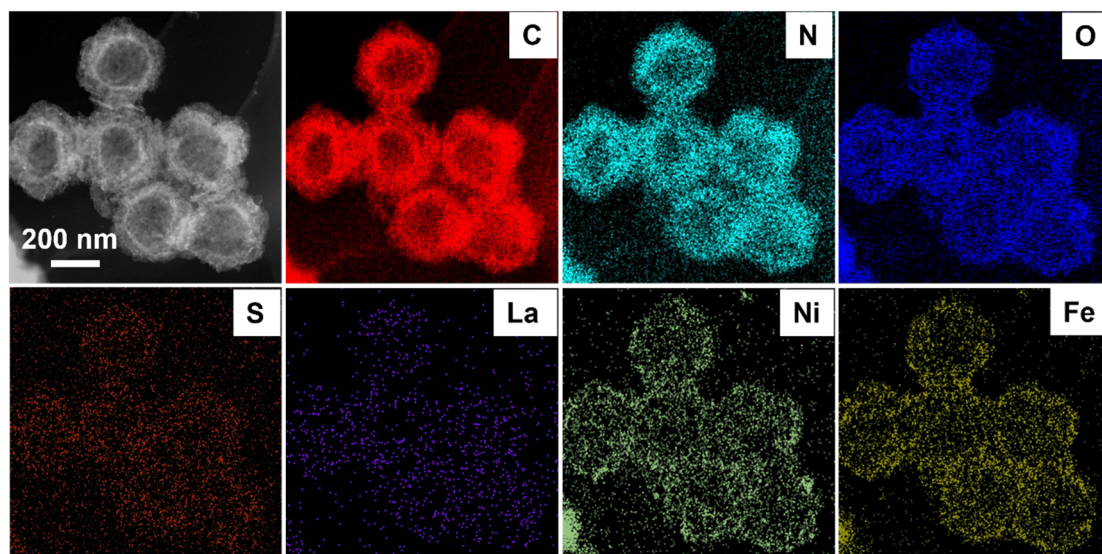


Fig. S28 Dark-field TEM image and corresponding EDS elemental mapping of NiFe-LDH@NHPC after 2000 CV cycles test.

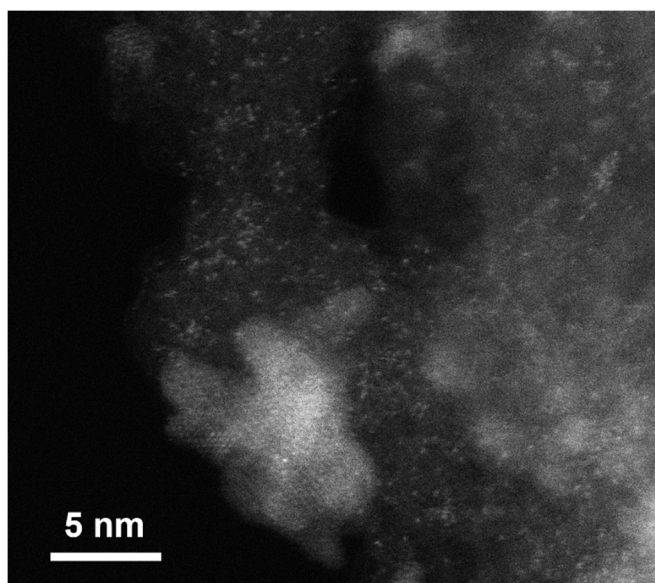


Fig. S29 AC-HAADF-STEM image of NiFe-LDH@NHPC after 2000 CV cycles test.

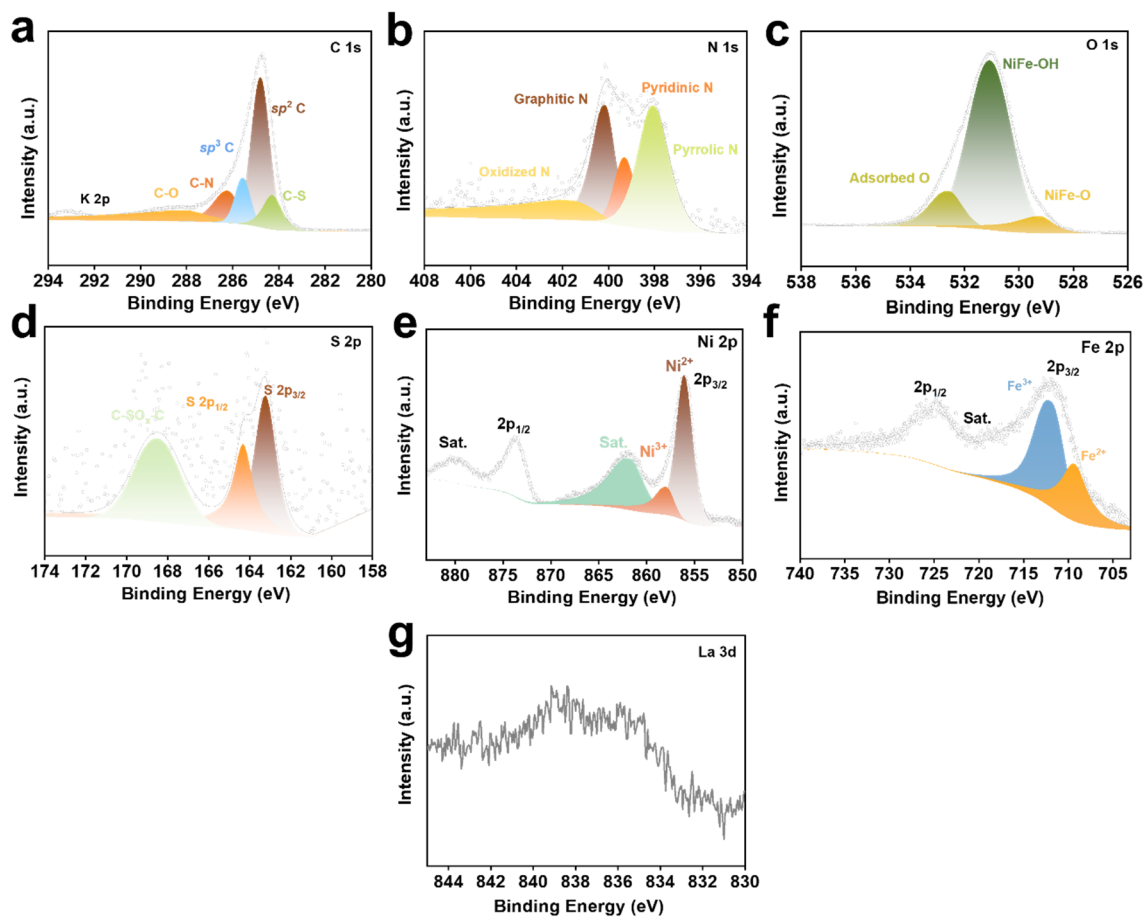


Fig. S30 The High-resolution XPS spectra for C 1s (a), N 1s (b) O 1s (c), S 2p (d), Ni 2p (e), Fe 2p (f), La 3d (g) of NiFe-LDH@La SNHPC after 2000 CV cycles OER test.

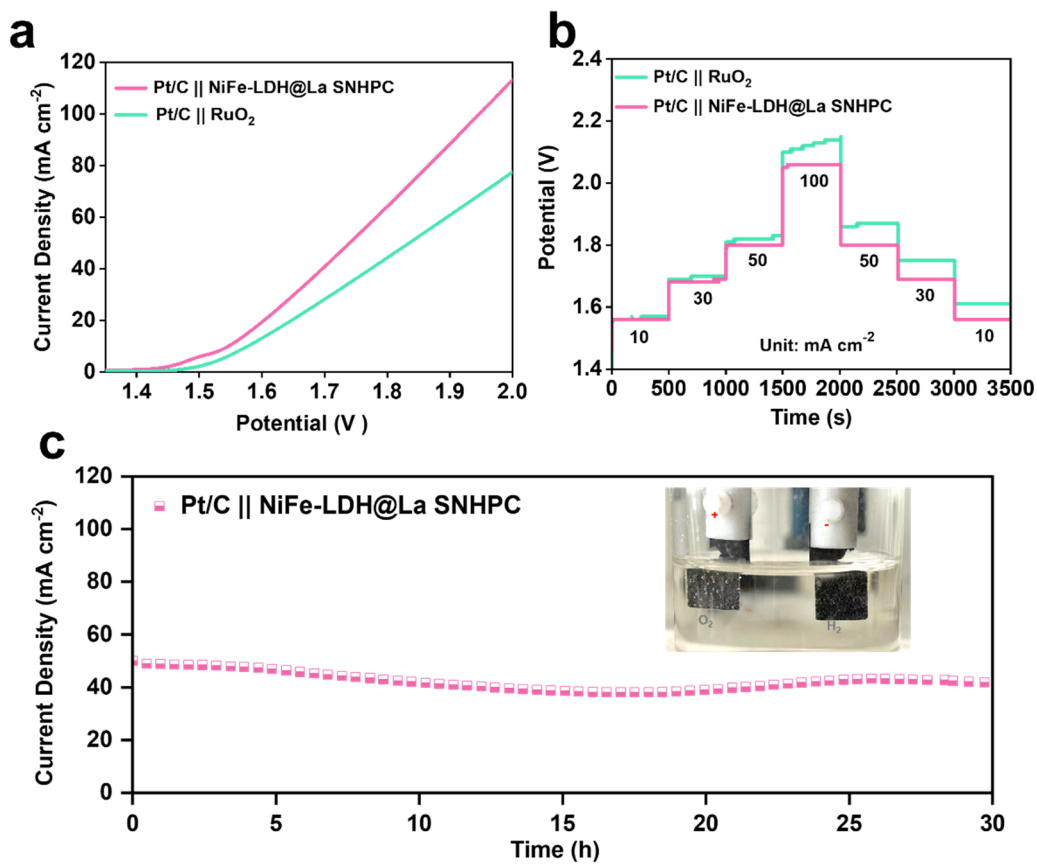


Fig. S31 LSV curves (a) and multi-step chronopotentiometry tests (b) of NiFe-LDH@La SNHPC||Pt/C and RuO₂||Pt/C couple in water splitting. (c) Chronopotentiometry stability a current density of 50 mA cm⁻² at 1.0M KOH.

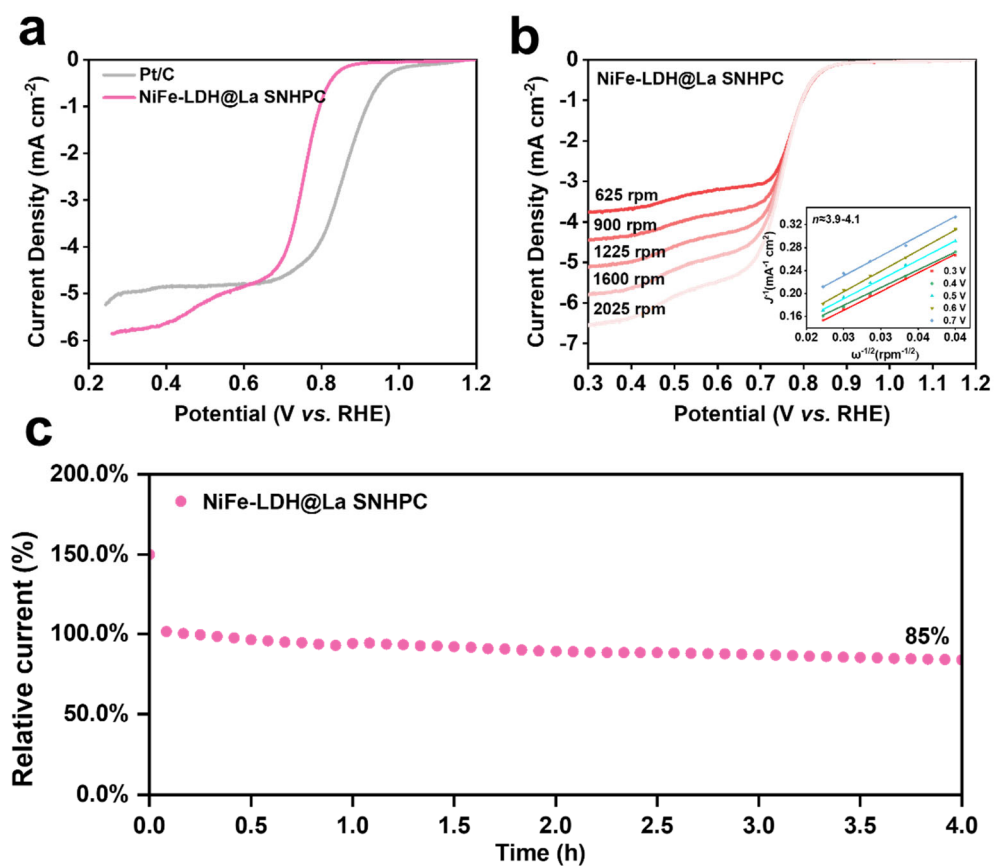


Fig. S32 (a) ORR LSV curves of NiFe-LDH@La SNHPC and Pt/C. (b) Rotation speed-dependent polarization curves of NiFe-LDH@La SNHPC and the corresponding K-L fitting lines at various potentials (inset). (c) The ORR chronoamperometric measurements of NiFe-LDH@La SNHPC in O_2 -saturated 0.1M KOH at 0.6 V.

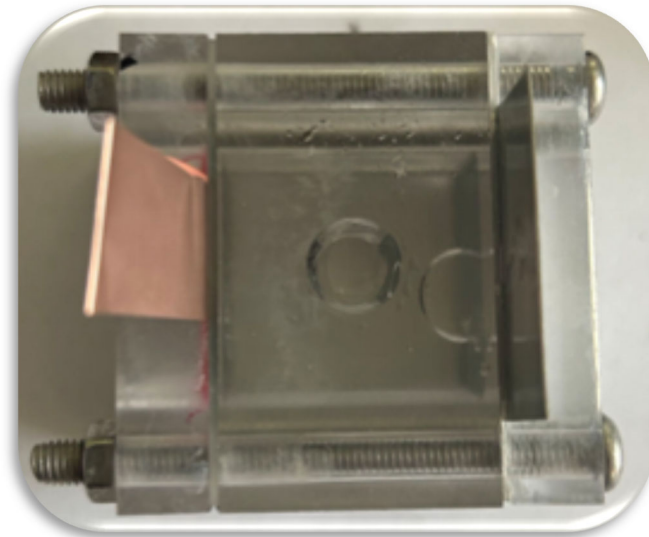


Fig. S33 Digital image of the assembled ZAB.

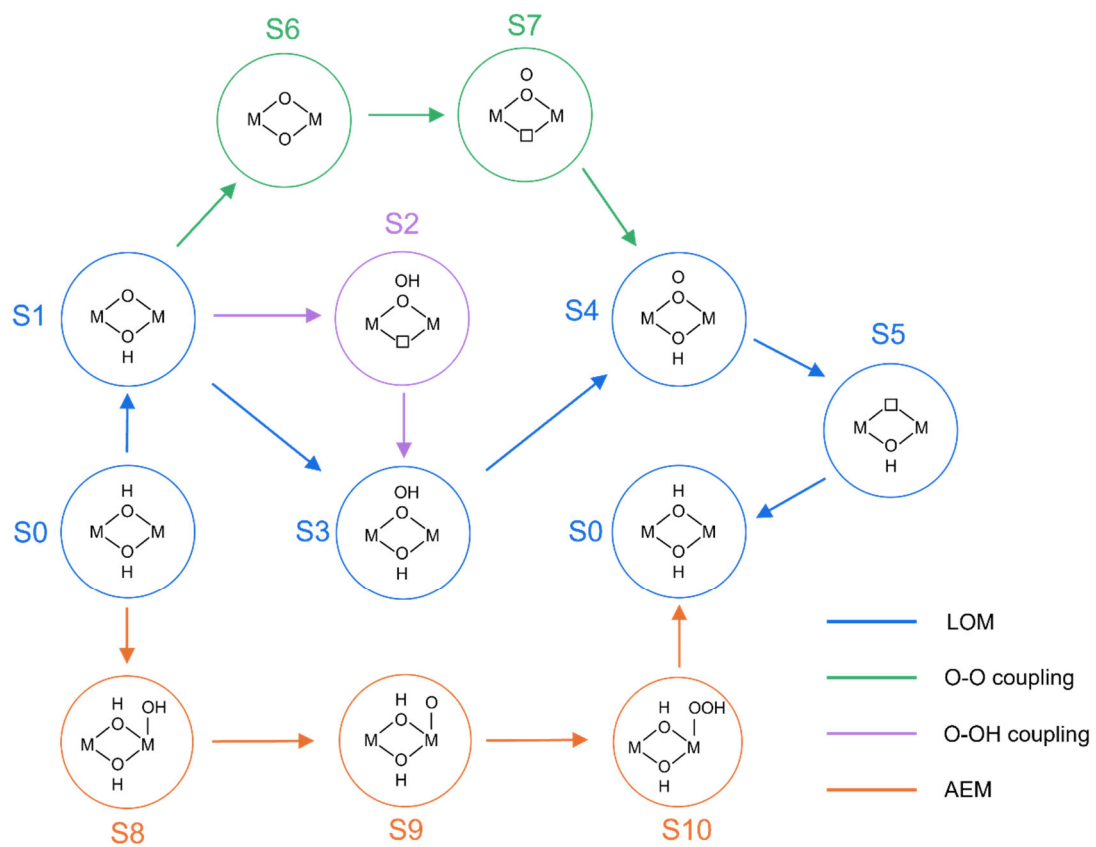


Fig. S34 The OER reaction pathways, including AEM, LOM, and O-O and O-OH coupling pathways.

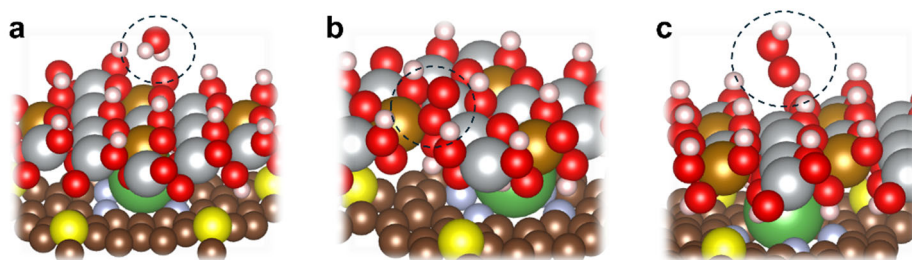


Fig. S35 Optimized structures of S8 (a), S9 (b), and S10 (c) in **Fig. S34** in AEM pathway for NiFe-LDH@La SNHPC.

The models of S8, S9, and S10 in the AEM pathway correspond to *OH , *O , and *OOH intermediates, respectively. But on the (001) facet of NiFe-LDH, each metal atom is coordinated to six oxygen atoms, with each O atom located at the hollow site of three underlying metal atoms. This structural arrangement makes it challenging for additional O species to form bonds, and there is insufficient space for O species to adsorb atop the metal atoms. This suggests that the conventional AEM pathway is unlikely to occur. Our optimized *OH is transferred to H_2O which is formed by *OH and original *H in LDH. The optimized *O adsorbs at an O site and transfers to *OO , corresponding to the S4 type intermediate, which then desorbs and participates in the LOM pathway. The optimized *OOH species is positioned far from the basal plane. As a result, we do not obtain the optimized structures for AEM intermediates adsorbing directly on metal atoms (S8, S9, and S10 type), which demonstrates that the AEM pathway is not present. And LOM pathway is more favorable on the (001) facet, consistent with previous literature¹². The white, coffee, blue, red, yellow, silver, brown, and green balls represent the H, C, N, O, S, Fe, Ni and La, respectively.

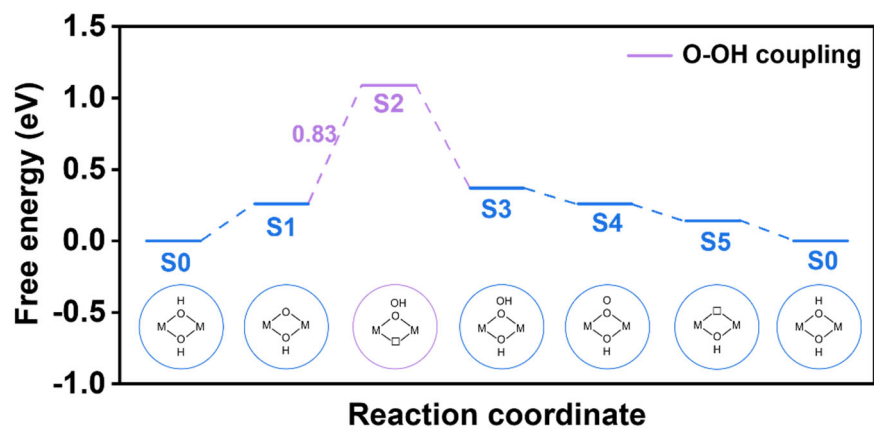


Fig. S36 Free energy diagram of O-OH coupling pathway at $U = 1.23$ V/RHE for NiFe-LDH@La SNHPC.

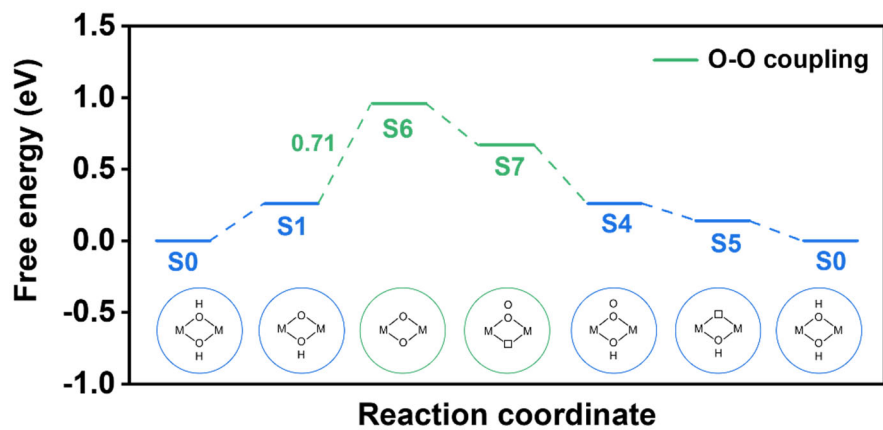


Fig. S37 Free energy diagram of O-O coupling pathway at $U = 1.23$ V/RHE for NiFe-LDH@La SNHPC.

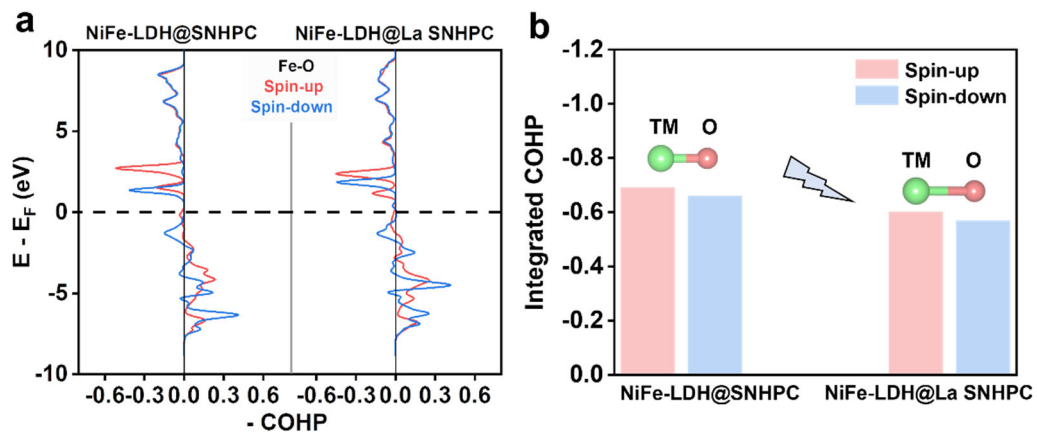


Fig. S38 (a) COHP of the Fe-O bond in NiFe-LDH@SNHPC and NiFe-LDH@La SNHPC and (b) the values of integrated COHP.

Table S1. EXAFS fitting parameters at the La L₃-edge for various samples.

Sample	Shell	CN	R (Å)	σ^2 (Å ² ·10 ⁻³)	ΔE_0 (eV)	R factor (%)
La ₂ O ₃	La-O1	3	2.44±0.01	0.0159	7.8±1.1	1.67
	La-O2	3	2.77±0.01	0.0121		
	La-La1	3	3.55±0.01	0.0131		
	La-La2	6	3.90±0.01	0.0091		
NiFe-LDH@La SNHPC	La-N	4.0	2.60	3.07	14.57	1.8

CN is the coordination number; R is interatomic distance (the bond length between central atoms and surrounding coordination atoms); σ^2 is Debye-Waller factor (a measure of thermal and static disorder in absorber-scatterer distances); ΔE_0 is edge-energy shift (the difference between the zero kinetic energy value of the sample and that of the theoretical model). R factor is used to value the goodness of the fitting.

Table S2. Summary of OER performance for some reported NiFe-based catalysts in alkaline solution.

Catalyst	Overpotential at 10 mA cm ⁻²	Tafel slope (mV dec ⁻¹)	Substrate	Loading Capacity (mg cm ⁻¹)	Reference
NiFe-LDH@La SNC	251	53.2	CP	0.6	This work
NiFe-LDH/Fe ₁ -N-C	320	41	GC	0.3	<i>Adv. Energy Mater.</i> , 2023 , 13, 2203609.
NiFe-ANR	228	37	GC	-	<i>Angew. Chem. Int. Ed.</i> 2023 , 62, e202300478.
Nd/Co@NC	288	90.7	GC	~0.71	<i>Adv. Energy Mater.</i> 2023 , 13, 2203244.
P-Ce SAs@CoO	261	75	CC	~0.5	<i>Adv. Mater.</i> 2023 , 2302462
Ce-CoP@CC	240	50.39	CC	-	<i>Adv. Energy Mater.</i> 2023 , 13, 2301162.
Fe-NiO-Ni CHNAs	245	43.4	CC	-	<i>App. Catal. B: Environ.</i> , 2021 , 285, 119809.
FeNi SAs/NC	270	55	NF	1.0	<i>Adv. Energy Mater.</i> , 2021 , 11, 2101242.
P-doped Ni-Fe-S microspheres	264	48	GC	0.3	<i>J. Power Sources</i> , 2021 , 490, 229552.
Fe-NiNC-50	340	54	GC	0.25	<i>Nano Energy</i> , 2020 , 71, 104597.
NiFe _{0.5} Sn-A	260	50	CC	-	<i>Adv. Sci.</i> , 2020 , 7, 1903777.
nNiFe LDH/3D MPC	340	71	GC	0.1	<i>J. Mater. Chem. A</i> , 2018 , 6, 14299-14306.
Ni-Fe LDH hollow nanoprisms	280	49.4	GC	0.16	<i>Angew. Chem. Int. Ed.</i> , 2018 , 130, 178 –182.
NiFe-LDH/Co, N-CNF	312	60	GC	0.12	<i>Adv. Energy Mater.</i> , 2017 , 7, 1700467.

GC, CP, CC, NF refer to glassy-carbon, carbon paper, carbon cloth and nickel foam respectively.

Table S3. Each term for free energy correction which is printed by VASPKIT package.

	ZPE/eV	TS/eV	$\int_0^T C_p dT/eV$	G/eV
*OO	0.13	0.14	0.07	0.06
*OOH	0.49	0.09	0.05	0.45
*O	0.07	0.04	0.02	0.05
*OH	0.38	0.06	0.04	0.36

Reference

1. Kresse, Furthmuller, *Phys. Rev. B: Condens. Matter* **1996**, *54*, 11169-11186.
2. Kresse, Hafner, *Phys. Rev. B: Condens. Matter* **1993**, *47*, 558-561.
3. Blochl, *Phys. Rev. B: Condens. Matter* **1994**, *50*, 17953-17979.
4. J. P. Perdew, K. Burke, M. Ernzerhof, *Phys. Rev. Lett.* **1996**, *77*, 3865.
5. H. J. Monkhorst, J. D. Pack, *Phys. Rev. B: Condens. Matter* **1976**, *13*, 5188.
6. V. Wang, N. Xu, J.-C. Liu, G. Tang, W.-T. Geng, *Comput. Phys. Commun.* **2021**, *267*, 108033.
7. Z. Zeng, M. K. Y. Chan, Z.-J. Zhao, J. Kubal, D. Fan, J. Greeley, *J. Phys. Chem. C* **2015**, *119*, 18177-18187.
8. Z. Wang, W. A. Goddard, III, H. Xiao, *Nat. Commun.* **2023**, *14*, 4228.
9. F. Dionigi, Z. Zeng, I. Sinev, T. Merzdorf, S. Deshpande, M. B. Lopez, S. Kunze, I. Zegkinoglou, H. Sarodnik, D. Fan, A. Bergmann, J. Drnec, J. F. de Araujo, M. Gliech, D. Teschner, J. Zhu, W.-X. Li, J. Greeley, B. Roldan Cuenya, P. Strasser, *Nat. Commun.* **2020**, *11*, 2522.
10. C. D. Van, S. Kim, M. Kim, M. H. Lee, *ACS Sustainable Chem. Eng.* **2023**, *11*, 1333-1343.
11. B. Ji, J. Gou, Y. Zheng, X. Pu, Y. Wang, P. Kidkhunthod, Y. Tang, *Adv. Mater.* **2023**, *35*, 2300381.
12. Z. He, J. Zhang, Z. Gong, H. Lei, D. Zhou, N. Zhang, W. Mai, S. Zhao, Y. Chen, *Nat. Commun.* **2022**, *13*, 2191.